Reproducibility of Non-X-ray Background for the X-ray Imaging Spectrometer aboard Suzaku

Noriaki TAWA¹, Kiyoshi HAYASHIDA¹, Masaaki NAGAI¹, Hajime NAKAMOTO¹,
Hiroshi TSUNEMI¹, Hiroya YAMAGUCHI², Yoshitaka ISHISAKI³, Eric MILLER⁴,
Tsunefumi MIZUNO⁵, Tadayasu DOTANI⁶, Masanobu OZAKI⁶, and Haruyoshi KATAYAMA⁷

¹Department of Earth and Space Science, Graduate School of Science, Osaka University, Toyonaka,
Osaka 560-0043

tawa@ess.sci.osaka-u.ac.jp

²Department of Physics, Graduate School of Science, Kyoto University, Sakyo-ku, Kyoto 606-8502 ³Department of Physics, Tokyo Metropolitan University, 1-1 Minami-Osawa, Hachioji, Tokyo 192-0397

⁴Kavli Institute for Astrophysics and Space Research, Massachusetts Institute of Technology, Cambridge, MA 02139, USA

⁵Department of Physical science, Hiroshima University, 1-3-1 Kagamiyama, Higashi-Hiroshima, Hiroshima 739-8526

⁶Institute of Space and Astronautical Science, Japan Aerospace Exploration Agency, 3-1-1 Yoshino-dai, Sagamihara, Kanagawa 229-8510

⁷ Japan Aerospace Exploration Agency (JAXA), 2-1-1 Sengen, Tsukuba, Ibaraki 305-8505

(Received; accepted)

Abstract

One of the advantages of the X-ray Imaging Spectrometer (XIS) system on board Suzaku is its low and stable non-X-ray background (NXB). In order to make the best use of this advantage, modeling the NXB spectra with high accuracy is important to subtract them from the spectra of on-source observations. We construct an NXB database by collecting XIS events when the dark Earth covers the XIS FOV. The total exposure time of the NXB data is about 785 ks for each XIS. It is found that the count rate of the NXB anti-correlates with the cut-off-rigidity and correlates with the count rate of the PIN upper discriminator (PIN-UD) in Hard X-ray Detector on board Suzaku. We thus model the NXB spectrum for a given on-source observation by employing either of these parameters and obtain a better reproducibility of the NXB for the model with PIN-UD than that with the cut-off-rigidity. The reproducibility of the NXB model with PIN-UD is 4.55-5.63% for each XIS NXB in the 1-7 keV band and 2.79-4.36% for each XIS NXB in the 5-12 keV band for each 5 ks exposure of the NXB data. This NXB reproducibility is much smaller than the spatial fluctuation of

the cosmic X-ray background in the 1-7 keV band, and is almost comparable to that in the 5-12 keV band.

Key words: instrumentation: detectors — methods: data analysis — X-rays: general

1. Introduction

The X-ray Imaging Spectrometer (XIS) at the foci of the four X-ray telescopes (XRT) on board the Suzaku observatory are best suited in the recent X-ray astronomy satellites such as ASCA (Burke et al. 1991), Chandra (Weisskopf et al. 2002), and XMM (Lumb et al. 2000) for diffuse and low surface brightness sources owing to their large collection area and low and stable background level. One of the XIS, XIS1, has a back-illuminated (BI) CCD, while the other three XIS, XIS0, 2, 3, are equipped with front-illuminated (FI) CCDs (hereafter referred to as XIS-FIs; Koyama et al. 2007). The background levels normalized by the effective area and the field of view (FOV), in terms of the S/N ratio to diffuse emissions, of the XIS-FIs are comparable to those of the ASCA SIS (Mitsuda et al. 2007). Moreover, these background levels are ~ 3 and ~ 10 times lower than those of the XMM EPIC and the Chandra ACIS at 5 keV, respectively (Mitsuda et al. 2007).

The background of the XIS consists of three components: (1) non-X-ray background (NXB); (2) a solar component, which is emission from the earth's atmosphere illuminated by the Sun and solar wind charge exchange; and (3) a diffuse X-ray component from such sources a local hot bubble (LHB), galactic diffuse X-ray emissions, and cosmic X-ray background (CXB).

While the X-ray background is produced by emission within the XRT FOV, the XIS NXB is caused by charged particles and γ -rays (Mizuno et al. 2004) entering the detector from various directions. Therefore, the NXB varies with time according to the radiation environment of the satellite, i.e. the particle or γ -ray spectra hitting on Suzaku. Since the altitude of orbit of Suzaku is lower than that of XMM or Chandra, the particle and γ -ray spectra of Suzaku are different from that of XMM or Chandra. Although these spectra are not entirely clear, their intensities of Suzaku are relatively lower and more stable than those of XMM or Chandra. In the case of XMM EPIC, solar soft protons produce flares of up to 10 times of the quiescent background level and affect 30-40% of XMM observation time (Carter et al. 2007). However, this component hardly affects Suzaku.

The solar component (2) includes the fluorescence lines of nitrogen and oxygen from the earth atmosphere and scattered solar X-rays. The intensity of the solar component depends both on the solar activity and on the elevation angle from the sunlit earth edge. This component can be minimized by filtering the data based on the elevation angle from the sunlit earth edge. Emission lines of nitrogen and oxygen are enhanced through charge exchange between interplanetary and geocoronal neutral atoms and metal ions in the solar wind (Fujimoto et al.

2007). Referring to the solar wind data, proton or X-ray fluxes, helps the evaluation of this component.

The spectrum of the CXB is approximated a power-law spectrum of photon index of ~ 1.4 in 2-10 keV band (Kushino et al. 2002). The CXB is known to be a collection of faint unresolved extragalactic sources (Hasinger et al. 2001). It is uniform over the sky with some fluctuation. The LHB and galactic diffuse X-ray emissions are dominant below 1 keV, and their spectra depend on the direction of the sky. Snowden et al. (1997) proposed a model which provides their spectra based on the ROSAT all sky survey.

Among the three components of the XIS background, the solar component is time variable and most difficult to model. We try to minimize it by using the orbital and altitude data, which are elevation angles from the day or night Earth edge, and the solar wind data. The diffuse X-ray component is basically stable and can be evaluated by observation of other fields by Suzaku. The target of this paper is to properly estimate the NXB so that we can use it as a background model. It is most important to establish a method to accurately evaluate the NXB spectra and time variations in order to maximize the advantage of the low background level of the XIS. We thus construct an XIS NXB database to be used in the evaluation of the NXB and introduce a method to generate the NXB model given the intensity of charged particles. We also examine and confirm the reproducibility of our NXB model.

2. NXB of the XIS

2.1. NXB database

We constructed the database of the XIS NXB from the events collected while Suzaku was pointed toward the night Earth (NTE). Under this condition, the diffuse X-ray component (3) is blocked, and the solar component (2) does not contaminate. The criteria with which we selected the NTE events are as follows.

- Rev0.7 products (Mitsuda et al. 2007) of which the XIS mode was normal 5×5 or 3×3 mode (without burst or window options). The events were further filtered with the condition of T_SAA_HXD > 436 s, where T_SAA_HXD means time after the passage of the south atlantic anomaly (SAA). This criterion is used in revision 1.2 or 1.3 products (Mitsuda et al. 2007), and this filtering excludes flares in the NXB intensity just after Suzaku passed through the SAA. The events during the telemetry saturation were also excluded.
- Cleansis in FTOOLS was applied with the default parameters to exclude the flickering pixels.
- The NTE events were extracted for Earth elevation angles (ELV) less than -5° and Earth day-time elevation angles (DYE_ELV) greater than 100° .

Since the XIS was in initial operation during August 2005, we collected the NTE events from

data observed between September 2005 and May 2006 with the above criteria. The total exposure time of the NTE data is $\sim 785\,\mathrm{ks}$ for each XIS. The NXB database¹ consists of the NTE event files and the associated enhanced house keeping (EHK) file, in which orbital information is listed with time. Two associated tools, $mk_corsorted_spec_v1.0.pl$ and $mk_corweighted_bgd_v1.1.pl$, to generate the NXB model using the cut-off-rigidity were also prepared. Since the event files in the database can be processed with various FTOOLS including XSELECT, the NXB spectra can be easily created. The subject of this paper is to generate the most appropriate NXB spectra for a given observation.

We hereafter refer to the "NTE events" as the NXB events and refer to the data comprising the NXB events as the "NXB data". Additionally, the "NXB database" indicates the data set which contains the NXB event files and the associated EHK file.

2.2. NXB spectra

Figure 1 shows the NXB spectra of XISO and XIS1. The spectra are extracted from the whole region of the CCD except for the calibration source regions (two corners of the CCD chip (Koyama et al. 2007)). The XIS FOV is ~ 287 arcmin², which is 91% of the FOV of the whole CCD chip. The spectra show fluorescence lines of Al, Si, Au, Mn, and Ni in the XIS and XRT. Table 1 shows the intensities of these emission lines, and table 2 shows the origin for each fluorescence line. The XISO has relatively strong Mn-K emission lines at 5.9 and 6.5 keV as shown in table 1. This is due to stray X-rays from the ⁵⁵Fe calibration source, although why the radiation is detected outside the calibration source regions remains unknown (Yamaguchi et al. 2006). Since the XIS-FIs have a thick neutral layer beneath the depletion layer, most of the background events generated by charged particles produce charge over many pixels and are rejected as ASCA grade 7 events². On the other hand, the XIS1 (BI-CCD) has a relatively thin depletion layer and almost no neutral layer, resulting in relatively many background events in grades 0, 2, 3, 4, and 6 (Yamaguchi et al. 2006). Therefore, the background count rate of the XIS1 is higher than those of the XIS-FIs, especially above ~ 7 keV as shown in Fig. 1.

2.3. Cut-off-rigidity and PIN-UD

Since the NXB is caused by charged particles, the NXB should depend on the intensity of charged particles striking Suzaku, and this is strongly correlated with the geomagnetic cut-

The first version of the database is accessible via Suzaku web page at ISAS/JAXA (http://www.astro.isas.jaxa.jp/suzaku/analysis/xis/nte/) and GSFC/NASA (http://heasarc.gsfc.nasa.gov/docs/suzaku/analysis/xisbgd0.html), but the NXB data in this database lack T_SAA_HXD and telemetry saturation filtering described here, leading to a total exposure of 800 ks. The second version (the product of this paper) will be released in October 2007.

The ASCA grade shows the spread of an event. In the case of the XIS, we consider that most of the X-ray events do not split into a region larger than 2×2 pixels. Grade 7 events, in which the spread of event contains more than 2×2 pixels, are regarded as background events (Koyama et al. 2007).

Fig. 1. Spectra of the NXB in the XIS0 (black) and the XIS1 (gray).

Table 1. Energies and count rates of the line components in the NXB spectra.

				0 1 -	1.
Line	Energy	Count rate* $(10^{-9} \text{ cts s}^{-1} \text{ pixel}^{-1})$			
	(keV)	XIS0	XIS1	XIS2	XIS3
Al-K α	1.486	1.45 ± 0.11	1.84 ± 0.14	1.41 ± 0.10	1.41 ± 0.10
$\mathrm{Si}\text{-}\mathrm{K}\alpha$	1.740	0.479 ± 0.081	2.27 ± 0.15	0.476 ± 0.080	0.497 ± 0.082
$\mathrm{Au\text{-}M}\alpha$	2.123	0.63 ± 0.093	1.10 ± 0.13	0.776 ± 0.097	0.619 ± 0.092
$\mathrm{Mn}\text{-}\mathrm{K}\alpha$	5.895	6.92 ± 0.19	0.43 ± 0.14	1.19 ± 0.13	0.76 ± 0.11
$\operatorname{Mn-K}\!\beta$	6.490	1.10 ± 0.11	0.26 ± 0.13	0.40 ± 0.11	0.253 ± 0.094
Ni-K α	7.470	7.12 ± 0.19	7.06 ± 0.37	8.01 ± 0.20	7.50 ± 0.20
Ni-K β	8.265	0.96 ± 0.10	0.75 ± 0.22	1.16 ± 0.11	1.18 ± 0.11
$\mathrm{Au}\text{-}\mathrm{L}\alpha$	9.671	3.42 ± 0.15	4.15 ± 0.49	3.45 ± 0.15	3.30 ± 0.15
$\mathrm{Au}\text{-}\mathrm{L}\beta$	11.51	2.04 ± 0.14	1.93 ± 0.48	1.97 ± 0.14	1.83 ± 0.14

 $[\]overline{\ }^*$ The count rates are obtained from the whole CCD chip excluding the calibration source regions. Errors are 90 % confidence level.

Table 2. Origins of the fluorescence lines in the NXB spectra.

Line	Origin
$\mathrm{Al} ext{-}\mathrm{K}lpha$	Optical blocking filter, housing, alumina substrate to mount CCD
$\mathrm{Si}\text{-}\mathrm{K}lpha$	CCD (Si fluorescence line)
Au-M α , L α , L β	Housing, CCD substrate, heatsink
Mn-K α , K β	Scattered X-rays from calibration sources
Ni-K α , K β	Housing, heatsink

off-rigidity. We introduce a new type of cut-off-rigidity, COR2, for Suzaku. The calculation for the COR2 is independent from that for the conventional cut-off-rigidity, COR. The COR has been employed in the analysis of Tenma, Ginga, ASCA, and Suzaku. We summarize the characteristics of COR and COR2 in appendix 1. In the main text, we use COR2 when discussing the NXB.

Suzaku carries a non-imaging hard X-ray instrument, the Hard X-ray Detector (HXD). The HXD sensor contains 4×4 well-type phoswich units (well units) with 4 PIN silicon diodes in each (Takahashi et al. 2007, Kokubun et al. 2007). When a charged particle generates a large signal in a PIN silicon diode, the PIN upper discriminator (PIN-UD) is activated at a threshold around 90 keV. This can be a good monitor of the real-time intensity of the charged particles striking Suzaku. The number of PIN-UD counts is recorded with each well unit. We sum up the PIN-UD count rates for all well units and average them for each 32 seconds to reduce the statistical error. The typical number of PIN-UD counts in 32 seconds is ~ 5100 counts by summing up all well units. We hereafter call this count rate the PIN-UD. Figure 2 shows the PIN-UD as a function of the COR2. There is a strong anti-correlation between the PIN-UD and the COR2. However, the anti-correlation is widely distributed. This is because that the PIN-UD mirrors the real-time intensity of the charged particles, while the COR2 is calculated from a COR map (shown in Fig. 12(b)) and the orbital position of Suzaku. Therefore, the COR2 might not correctly reproduce the real-time intensity of the charged particles. In addition, some events deviate from the correlation as shown in the region of A and B of Fig. 2. The events in region A occurred just before Suzaku entered the SAA. The events in region B occurred at the time when Suzaku passed near the region of (longitude, latitude) = (350°, 19°). We assume that this is because the COR2 values in this region are approximately calculated as shown in appendix 1. However, the number of events in regions A and B is less than 1% of the total number of events. We will discuss which parameters of the COR2 or PIN-UD can correctly reproduce the NXB in the next section.

Figure 3(a) shows the count rate of the NXB for each XIS in the 5-12 keV energy band as a function of the COR2. The count rate of each bin of XIS1 is about 6 times higher than those of XIS-FIs. This is because the XIS1 has a relatively thin depletion layer and almost no neutral layer, as discussed in section 2.2. Therefore, the NXB intensity of XIS1 depends on the intensity of charged particles as well as the XIS-FIs. On the other hand, spectra are different between the low COR2 region ($COR2 \le 8$ GV) and high COR2 region ($COR2 \ge 8$ GV) as shown in Figure 3(b). The differences mainly appear in normalization of the spectra. The periods of the NXB variations primarily correspond to the orbital period of Suzaku, 96 minutes, since the NXB depends on the cut-off rigidity. We should also note that the NXB does not have apparent long-term changes in 9 months. For details, we will discuss in sections 3.3 and 4.

Since the COR2 and the NXB count rate are anti-correlated, we can use the COR2

Fig. 2. The PIN-UD as a function of the COR2. The PIN-UD is anti-correlated with the COR2, although there is noticeable scatter such as the region of A and B. The events in region A occurred just before Suzaku entered the SAA. The events in region B occurred at the time when Suzaku passed near the region of (longitude, latitude) = $(350^{\circ}, 19^{\circ})$.

to estimate the NXB spectra to be subtracted as background for a given observation. The PIN-UD can also be used as such a parameter to estimate the NXB spectra, considering the anti-correlation between the COR2 and the PIN-UD. In the following section, we will attempt to model the NXB spectra from the NXB data by employing either of the COR2 or the PIN-UD. The two kinds of NXB models, one with the COR2 and the other with the PIN-UD, will be compared by their reproducibilities.

Fig. 3. (a) COR2 dependence of the NXB (average count rate in 5-12 keV) for each XIS. (b) NXB spectra in $COR2 \le 8$ and COR2 > 8 GV. Black and red lines show the XIS0 spectra. Green and blue lines show the XIS1 spectra. The NXB count rate is anti-correlated with the COR2, and the count rate of XIS1 is higher than those of XIS-FIs.

3. NXB models and their Reproducibility

3.1. NXB models: NXB data sorted by COR2 or PIN-UD

In order to correctly subtract the NXB from on-source observation, we introduce method to model the NXB. Since the spectra of charged particles and γ -ray causing the NXB are not fully understood, this is a semi-empirical method. We prepared two tools, $mk_corsorted_spec$ and $mk_corweighted_bgd^3$, to generate the NXB model. $Mk_corsorted_spec$ is to sort with modeling parameter, i.e. COR2 or PIN-UD, bin and generates the NXB spectra for each modeling parameter bin. $Mk_corweighted_bgd$ is to generate the NXB model spectrum for a given on-source observation by summing up the sorted spectra with appropriate weights. The weighted NXB model spectrum, S_w , is expressed as follows,

$$S_w = \frac{\sum_{i=1}^n T_i S_i}{\sum_{i=1}^n T_i} = \sum_{i=1}^n \frac{T_i}{T_{total}} S_i , \qquad (1)$$

where the modeling parameter is sorted into n bins. T_i and S_i are the exposure time of the on-source observation and the spectrum of the NXB data in the ith modeling parameter bin, respectively. T_{total} is the total exposure time of the on-source observation. Equation (1) makes equal the modeling parameter distribution for the on-source observation and that for the NXB data.

We sorted the NXB and on-source data into 14 bins with either the COR2 or PIN-UD. The COR2 and PIN-UD bins are defined as shown in table 3. In addition, table 3 shows the NXB count rate (5-12 keV) and exposure time for each COR2 and PIN-UD bin in the XISO. We defined the bin ranges at even intervals of the PIN-UD and set the COR2 bins so as to get the approximately comparable count rate of the corresponding PIN-UD bins. We should note that the NXB model obtained by sorting into even intervals with the exposure time has comparable level to that by sorting into the bins shown in table 3.

3.2. Reproducibility of the NXB models

We first calculate the intrinsic variability of the NXB data to compare with the reproducibility of the NXB model. The standard deviation of the NXB count rate contains the systematic error and statistical error. We define the systematic error (1σ confidence level) as the intrinsic variability. To calculate the intrinsic variability, we divide the NXB data into 5 ks exposure bins (generally spanning a few days) and obtain the count rate for each. Since the NXB intensity is particularly low, the count rates are obtained in the 5-12 keV energy band to reduce the statistical error. There are typically 250 counts per 5 ks exposure bin in this energy range for the XIS-FIs. Figure 4 shows the distribution of this count rate, hereafter called C_i

These tools are new versions of $mk_corsorted_spec_v1.0.pl$ and $mk_corweighted_bgd_v1.1.pl$. $mk_corsorted_spec_v1.0.pl$ and $mk_corweighted_bgd_v1.1.pl$ support the COR only. We will merge the new tools in one and release it as xisnxbgen in FTOOLS.

Table 3. The PIN-UD and the COR2 bins ranges.

Bin #	PIN-UD	Count rate*	Exposure [†]	COR2	Count rate*	Exposure [†]
	$({\rm cts}\;{\rm s}^{-1})$	$10^{-2} ({\rm cts} {\rm s}^{-1})$	(ks)	$\overline{\text{(GV)}}$	$10^{-2} ({\rm cts} {\rm s}^{-1})$	(ks)
1	100-150	4.551 ± 0.051	175.4	15-12.8	4.746 ± 0.048	208.3
2	150-175	4.857 ± 0.045	236.6	12.8-10.5	4.877 ± 0.045	246.2
3	175-200	5.329 ± 0.062	137.7	10.5-9.1	5.347 ± 0.061	142.6
4	200-225	5.533 ± 0.089	70.0	9.1-8.1	5.73 ± 0.10	53.6
5	225-250	6.24 ± 0.15	28.3	8.1-7.3	6.24 ± 0.15	27.6
6	250 - 275	6.74 ± 0.18	20.7	7.3-6.6	6.49 ± 0.18	19.2
7	275-300	6.85 ± 0.20	17.9	6.6-6.0	7.17 ± 0.20	17.5
8	300-325	7.83 ± 0.23	14.3	6.0 - 5.5	7.29 ± 0.24	13.0
9	325-350	7.42 ± 0.23	13.6	5.5 - 5.1	7.83 ± 0.27	10.8
10	350-375	8.35 ± 0.26	12.5	5.1 - 4.7	7.52 ± 0.25	12.2
11	375-400	9.33 ± 0.27	12.4	4.7 - 4.3	8.60 ± 0.28	11.3
12	400-425	10.61 ± 0.31	10.8	4.3 - 4.0	9.55 ± 0.32	9.5
13	425-450	11.53 ± 0.48	4.9	4.0 - 3.7	11.37 ± 0.39	7.3
14	450-500	7.4 ± 1.3	0.4	3.7-2.0	13.74 ± 0.59	4.0

^{*} The count rates are obtained from the NXB data of the XIS0 in the 5-12 keV band. Errors are 1σ confidence level.

for the jth bin. We calculate the standard deviation of C_j (σ_c) as follows,

$$\sigma_c^2 = \frac{1}{n-1} \sum_{j=1}^n (C_j - \mu_c)^2 , \qquad (2)$$

where n is the number of the 5 ks NXB data, and μ_c is the average of C_i , $\mu_c = (1/N) \sum_{j=1}^n C_j$. Then, the statistical error of C_j is assumed by Poisson statistics and is calculated by $\sqrt{C_j/T_j}$, where T_j is a exposure time of the jth bin (in this case, T_j is 5 ks). Since we divided the NXB data into 5 ks exposure, the statistical error of each C_j is approximately constant. We therefore obtain the statistical error contained in σ_c ($\sigma_{sta,c}$) as follows,

$$\sigma_{sta,c} = \frac{1}{n} \sum_{j=1}^{n} \sqrt{\frac{C_j}{T_j}} \ . \tag{3}$$

We then calculate the systematic error $(\sigma_{sys,c})$ as follows,

$$\sigma_{sys,c} = \sqrt{\sigma_c^2 - \sigma_{sta,c}^2} \ . \tag{4}$$

 $\sigma_{sys,c}$ is the intrinsic variability and is summarized in table 4. The intrinsic variability shows the reproducibility of the NXB without being modeled. Details about the errors of σ_c , $\sigma_{sta,c}$, and $\sigma_{sys,c}$ shown in table 4, are presented in appendix 2.

We next calculate the reproducibility of NXB model described in eq. (1). The NXB

 $^{^\}dagger$ The exposure times are obtained from the NXB data of the XIS0.

spectra, S_i in eq. (1), are obtained from the NXB data according to the modeling parameter. The weights of each bin, T_i/T_{total} in eq. (1), are calculated by the modeling parameter for each 5 ks NXB data bin. We thus obtained the NXB models for each 5 ks bin and calculated the residual, data minus model. The jth residual (ΔC_j) is calculated by $C_j - M_j$, where M_j is the count rate of the NXB model for the jth 5 ks NXB data bin. There are two kinds of ΔC_j , ΔC_{COR2} and ΔC_{PIN-UD} , which are calculated based on the COR2 and the PIN-UD, respectively. Figure 5 shows the distributions of ΔC_{COR2} and ΔC_{PIN-UD} in the 5-12 keV energy band. These distributions are relatively narrow compared with the distribution of C_j shown in Fig. 4. This indicates that the NXB models correctly reproduce the NXB data. Since the way to calculate the reproducibility is the same with ΔC_{COR2} and ΔC_{PIN-UD} , we express this with ΔC_j . The standard deviation of ΔC_j ($\sigma_{\Delta c}$) is calculated as follows,

$$\sigma_{\Delta c}^{2} = \frac{1}{n-1} \sum_{j=1}^{n} (\Delta C_{j} - \mu_{\Delta c})^{2} , \qquad (5)$$

where $\mu_{\Delta c}$ is the average of ΔC_j and is expected to be zero. The statistical error of ΔC_j is $\sqrt{C_j/T_j + M_j/T}$, where T is total exposure time of the NXB data. The average of these statistical errors $(\sigma_{sta,\Delta c})$ is expressed as follows,

$$\sigma_{sta,\Delta c} = \frac{1}{n} \sum_{j=1}^{n} \sqrt{\frac{C_j}{T_j} + \frac{M_j}{T}} \ . \tag{6}$$

Since $T \sim 157T_j$, the value of $\sigma_{sta,\Delta c}$ is approximately $\sigma_{sta,c}$ (eq. (3)). By using $\sigma_{\Delta c}$ and $\sigma_{sta,\Delta c}$, the systematic error of ΔC_j ($\sigma_{sys,\Delta c}$) is calculated as follows,

$$\sigma_{sys,\Delta c} = \sqrt{\sigma_{\Delta c}^2 - \sigma_{sta,\Delta c}^2} \ . \tag{7}$$

Hear $\sigma_{sys,\Delta c}$ is defined as the "reproducibility" of the NXB model. We independently calculate the reproducibility for each XIS and show them in table 5(a). Details about the errors of the reproducibilities are presented in appendix 2. Since the PIN-UD sometimes exceeds the range of 100-500 cts s⁻¹, the total exposure time reduces to ~ 760 ks. On the other hand, for the NXB model with the COR2, the whole NXB data set of ~ 785 ks is available. The reproducibilities of the NXB models (table 5(a)) are about 1/3 of the intrinsic variability of the NXB count rate (table 4). However, the residuals sometimes becomes large in both NXB models, as shown in Fig. 5.

3.3. Improvements to the NXB model by filtering the data

To further improve the reproducibilities of the NXB models, we examined the time and orbital position of Suzaku when the count rate significantly deviates from the NXB model, i.e. $> 0.01 \text{ cts s}^{-1}$ for the XIS-FIs in Fig. 5. We found that those data are obtained from 2005/10/09 ($t = 1.822 \times 10^8 \text{ s}$, where t is time since $2000/01/01 \ 00:00:00$) to $2005/10/28 \ (t = 1.838 \times 10^8 \text{ s})$ and from $2005/11/29 \ (t = 1.866 \times 10^8 \text{ s})$ to $2005/12/20 \ (t = 1.884 \times 10^8 \text{ s})$. We call these time periods period-A. Figure 6 shows the light curve of ΔC_{PIN-UD} . The count rate of ΔC_{PIN-UD}

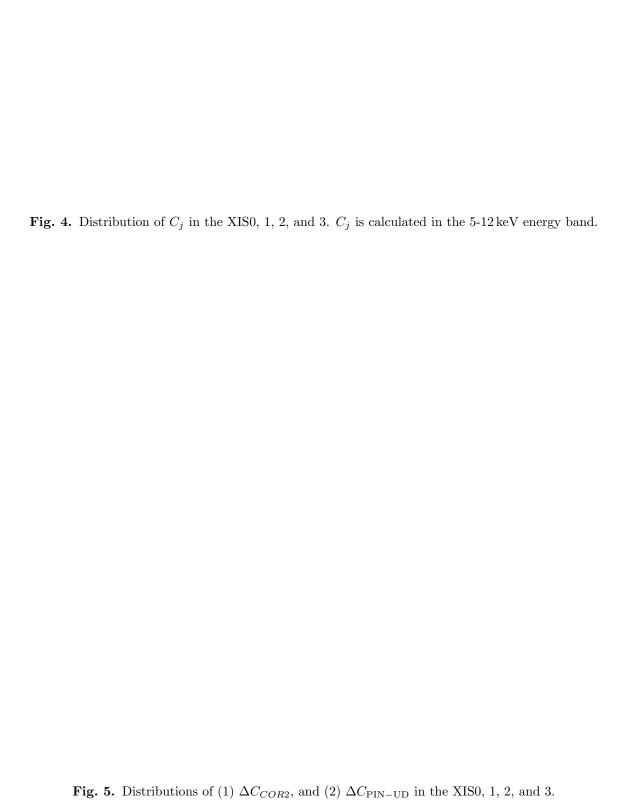


Table 4. Statistical summary of the NXB data.

Sensor	Average count rate*	Standard deviation [†]	Statistical error [†]	Intrinsic variability †
	$10^{-2} ({\rm cts} {\rm s}^{-1})$	(%)	(%)	(%)
XIS0	5.464 ± 0.026	19.2 ± 1.1	6.03 ± 0.34	18.2 ± 1.1
XIS1	28.758 ± 0.060	22.5 ± 1.3	2.62 ± 0.15	22.4 ± 1.3
XIS2	5.317 ± 0.026	19.1 ± 1.1	6.11 ± 0.35	18.1 ± 1.1
XIS3	4.685 ± 0.024	16.85 ± 0.95	6.51 ± 0.37	15.5 ± 1.0

^{*} The count rates are obtained from the NXB data in the 5-12 keV band. Errors are 1σ confidence level.

increase at the first time period of period-A, especially in the XISO.

Figure 7(a) shows the orbital position during period-A, and Fig. 7(b) shows the orbital position at other times. These plots indicate that the residuals increase when Suzaku passes through high latitude and high altitude region. We therefore exclude the NXB events during the time when the orbital positions of Suzaku were latitude $\leq -23^{\circ}$, altitude ≥ 576.5 km or latitude $\geq 29^{\circ}$, altitude ≥ 577.5 km (hereafter the "orbit filter") from the NXB data. The total exposure time of the NXB data with the orbit filter (hereafter "NXB1") is ~ 730 ks, while that with the PIN-UD is ~ 710 ks. The reproducibilities of the NXB models for the NXB1 data are independently evaluated for each XIS by the same way as that in section 3.2 . Figure 8(a) shows the distribution of $\Delta C_{\text{PIN-UD}}$ obtained from the NXB1 data, and table 5(b) shows their reproducibilities. We can improve reproducibilities by employing the orbit filter. Especially, the reproducibility of the XIS0 is 3 times better than that without orbit filter.

The NXB model of XIS2 with the orbit filter applied has almost the same level of the reproducibility as that without the orbit filter. In addition, the reproducibility of XIS2 is the worst among the XIS-FIs (XIS0, 2, 3) (table 5(a) and (b)). We therefore investigate the long-term variation of the NXB intensity. Figure 9 shows the light curve of $\Delta C_{\text{PIN-UD}}$ obtained from the NXB1 data. We found that $\Delta C_{\text{PIN-UD}}$ during September 2005 had been higher than that after October 2005, especially in the XIS2. We speculate that this is because the solar activity was particularly high during September 2005. The proton and solar X-ray intensities are continuously monitored by the Geostationary Operational Environmental Satellites (GOES)⁴. These intensities in September 2005 frequently exceeded 100 times those of the normal state of the Sun. We fitted the light curve after October 2005 with a linear function, finding that the NXB intensities of the XIS-FIs were constant with time within $\pm 6\%$ per year. On the other hand, the NXB intensity of XIS1 decreased with a gradient of $(-7.8 \pm 5.8)\%$ per year (90% confidence level). However, since the gradient is small, we continue to apply the same method of modeling as the XIS-FIs to XIS1.

We therefore exclude the NXB events during September 2005 from the NXB1 data

[†] These values are normalized by the average count rate.

⁴ The GOES data are available at \(\lambda\text{http://www.ngdc.noaa.gov/stp/GOES/goes.html}\)

(hereafter "NXB2") and independently evaluate their reproducibilities for each XIS. Figure 8(b) shows the distribution of $\Delta C_{\text{PIN-UD}}$ obtained from the NXB2 data, and table 5(c) shows their reproducibilities. Better reproducibilities than the unfiltered NXB data can be obtained for all the XIS. In addition, we found that the NXB model with the PIN-UD has better reproducibility than that with the COR2. The total exposure time of this NXB2 data is $\sim 560\,\mathrm{ks}$, but for the PIN-UD model, the exposure time is $\sim 550\,\mathrm{ks}$. Since the exposure time is long enough, excluding the data during September 2005 is not a serious problem for the observations after October 2005.

Fig. 6. Light curve of $\Delta C_{\text{PIN-UD}}$ in the XISO, 1, 2, and 3. The residuals are obtained from the unfiltered NXB data in the 5-12keV band.

Fig. 7. Orbital positions of Suzaku for XIS observations of the NTE during (a) period-A and (b) other times.



Table 5. Reproducibilities of two kinds of the NXB models which are calculated for the 5 ks NXB data in the 5-12 keV energy band.

NXB	Sensor	COR2* (%)	PIN-UD* (%)
(a) Unfiltered	XIS0	6.60 ± 0.61	8.12 ± 0.68
	XIS1	7.18 ± 0.46	5.57 ± 0.39
	XIS2	10.33 ± 0.77	7.85 ± 0.68
	XIS3	3.32 ± 0.56	3.42 ± 0.57
(b) <i>NXB1</i>	XIS0	4.05 ± 0.55	2.67 ± 0.53
	XIS1	6.32 ± 0.43	4.81 ± 0.36
	XIS2	9.77 ± 0.76	8.49 ± 0.72
	XIS3	4.09 ± 0.59	4.11 ± 0.60
(c) <i>NXB2</i>	XIS0	3.54 ± 0.61	2.79 ± 0.60
	XIS1	6.95 ± 0.53	4.36 ± 0.39
	XIS2	5.67 ± 0.69	3.96 ± 0.64
	XIS3	2.34 ± 0.64	3.82 ± 0.68

^{*} These values are normalized by the average count rate shown in table 4. Errors are 1σ confidence level.

3.4. Reproducibility of the NXB for the 1-7keV band

We evaluate the reproducibility of the NXB in the 1-7 keV energy band by the same method as that in section 3.2. The CXB is dominant compared with the NXB in this energy band. Table 6 shows the average count rate, statistical error, and reproducibility for the 5 ks NXB2 data. The reproducibilities are as good as those for the 5-12 keV energy band (table 5(c)), and the NXB model with the PIN-UD has better reproducibility than that with the COR2.

Table 6. Reproducibilities of the NXB models which are calculated by dividing the NXB2 data into 5 ks exposure bins in the 1-7 keV energy band.

Sensor	Average count rate	Statistical error*	Reprod	lucibility*
	$10^{-2} ({\rm cts} {\rm s}^{-1})$	(%)	COR2~(%)	PIN-UD (%)
XIS0	4.163 ± 0.027	6.94 ± 0.47	5.06 ± 0.74	4.55 ± 0.74
XIS1	7.321 ± 0.036	5.22 ± 0.35	7.55 ± 0.71	5.63 ± 0.63
XIS2	3.871 ± 0.026	7.19 ± 0.49	7.31 ± 0.84	5.18 ± 0.78
XIS3	3.475 ± 0.025	7.59 ± 0.52	6.34 ± 0.84	4.76 ± 0.80

^{*} These values are normalized by the average count rate. Errors are 1σ confidence level.

3.5. Reproducibility with longer exposure data

We have so far calculated the NXB reproducibility by dividing the NXB data into each 5 ks exposure bins. Here we examine the NXB reproducibility for a longer exposure time of 50 ks, typical for on-source observations. Each 50 ks NXB exposure typically spans a few weeks. Table 7 shows the reproducibilities of the NXB models for the exposure time of 50 ks in the energy bands of 1-7 keV and 5-12 keV. The reproducibilities of the 50 ks NXB models are improved from those for the 5 ks NXB models. This is because fluctuations of the residuals are smoothed by integrating for a long time.

Table 7. Reproducibilities of the NXB n	models which are calculated by dividing the	NXB2 data into 50 ks exposure bins.
--	---	-------------------------------------

Energy range	Energy range Sensor		Reprod	lucibility*
(keV)		(%)	COR2~(%)	PIN-UD (%)
1 - 7	XIS0	2.29 ± 0.54	1.89 ± 0.84	2.02 ± 0.90
	XIS1	1.72 ± 0.39	2.61 ± 0.80	2.70 ± 0.81
	XIS2	2.37 ± 0.56	1.73 ± 0.84	0.31 ± 0.79
	XIS3	2.50 ± 0.59	2.08 ± 0.92	1.20 ± 0.88
5 - 12	XIS0	1.96 ± 0.46	1.03 ± 0.66	1.89 ± 0.79
	XIS1	0.85 ± 0.19	2.98 ± 0.72	2.36 ± 0.59
	XIS2	1.98 ± 0.47	1.87 ± 0.75	1.20 ± 0.72
	XIS3	2.14 ± 0.50	1.51 ± 0.75	0.40 ± 0.72

^{*} These values are normalized by the average count rate in the energy bands of the 1-7 keV (table 6) or the 5-12 keV (table 4). Errors are 1σ confidence level.

4. Subtraction of the NXB from on-source observation

In this section, we consider the practical manner of how to subtract the NXB for on-source science observations. First, since the intensity of the NXB is not uniform over the CCD chip (Yamaguchi et al. 2006), the NXB spectrum needs to be extracted from the same region as the source spectrum in detector (DET) coordinates (Ishisaki et al. 2007). We can extract the NXB spectra sorted by the cut-off-rigidity for a given region defined in the DET coordinate with the $mk_corsorted_spec$ (same applies to the $mk_corsorted_spec_v1.0.pl$). Next, the sorted NXB spectra are summed up with appropriate weights calculated for the on-source observation using the $mk_corweighted_bgd$ (same applies to the $mk_corweighted_bgd_v1.1.pl$). The summed-up spectrum is the NXB model to be subtracted from on-source spectra.

One of the problems in this procedure is the presence of emission line components in the NXB spectra. These components are time-dependent; the energy resolution of the XIS degrades with time (Koyama et al. 2007), and the intensities of the Mn-K emission lines decrease with the half life of ⁵⁵Fe, 2.73 years. Since the NXB data contained in the NXB database are made from

the NXB events between September 2005 and May 2006 and this time dependence is not taken into account, the emission line components in the NXB spectra cannot be reproduced correctly for a given on-source observation. This problem becomes prominent for the observations after June 2006. Figure 10 shows an example of a raw on-source spectrum and the NXB model spectrum which we have described above. These are the averaged spectra of the XIS-FIs. Figure 11(a) shows the on-source spectrum from which the NXB model spectrum is subtracted, black minus red line shown in Fig. 10. This on-source spectrum is obtained in the observation of the link region between the galaxy clusters A 399 and A 401 taken during August 19-22 2006 with an exposure time of 150 ks (observation ID is 801020010. For details, see Fujita et al. 2007). The model in Fig. 11(a) is a single thermal model (APEC in XSPEC) plus power-law model. The thermal model represents the intracluster medium, and the power-law model represents the CXB. These are same models used by Fujita et al. (2007). Significant residuals are visible at the energies of Mn-K α (5.9 keV) and Ni-K α (7.4 keV) in Fig. 11(a). We have therefore developed a way to deal with these emission line components in the NXB spectra, as follows:

- 1. The NXB model spectrum is constructed with the *COR2* or the PIN-UD using the method described in subsection 3.1.
- 2. The line components Mn-K α , Mn-K β , Ni-K α , Ni-K β , and Au-L α , in the NXB model spectrum are fitted with the redistribution matrix file (RMF) for August 2005 observations, at which point the degradation of the energy resolution was negligible. For example, in the energy range of 5.5-7.0 keV where there are Mn-K α and Mn-K β lines, the spectrum is fitted with two Gaussians plus a power-law continuum. We have set the line widths of the two Gaussian components as free parameters. The emission lines of Ni-K α , Ni-K β , and Au-L α are similarly fitted.
- 3. We simulate the spectrum of the five Gaussian components using the *fakeit* command in XSPEC, using the fitting parameters determined in step 2.
- 4. The spectrum created in the step 3 is subtracted from the NXB model spectrum from step 1. This should correspond to the NXB continuum spectrum from which the five Gaussian line components are removed.
- 5. We add the simulated line components to the NXB continuum spectrum created in step 4, using the *fakeit* command. To take into account the degradation of energy resolution, this simulation needs to be done with the RMF calculated for the epoch of the on-source observation by using the *xisrmfgen* command in FTOOLS. *Xisrmfgen* is a response generator for the Suzaku XIS. The normalizations and line center energies of the five Gaussian components are fixed with those obtained in step 2, though radioactive decay of ⁵⁵Fe is taken into account. The intrinsic widths of these lines are fixed to be zero. We then get the NXB model spectrum in which degradation in the energy resolution and the ⁵⁵Fe decay are taken into account.

The NXB model spectrum with the correction for the emission line components is shown

as a green line in Fig. 10. The line widths of this spectrum are larger than those of the NXB model spectrum without the correction (red line shown in Fig. 10). Additionally, the intensities of Mn-K lines decrease with the correction. Figure 11(b) shows the source spectrum from which the NXB model with the correction for the emission line components is subtracted. The model in Fig. 11(b) is the same as that in Fig. 11(a). This correction can reduce the residuals in the energy bands including Mn-K α and Ni-K α , improving the reduced χ^2 from 1.77 to 1.16, in this case.

Fig. 10. (black) On-source observation spectrum. (red) The NXB model spectrum without the correction for the emission line components. (green) The NXB model spectrum with the correction for the emission line components. These are averaged spectra of the XIS-FIs.

Fig. 11. On-source observation with or without the correction for the emission line components. (a) The spectrum from which the NXB model spectrum is subtracted without the correction for the emission line components. (b) The spectrum from which the NXB model spectrum is subtracted with the correction for the emission line components. These are averaged spectra of the XIS-FIs.

5. Discussion

5.1. Case study: 100 ks exposure

In this section, we demonstrate to what extent the uncertainty of the source intensity depends on the NXB reproducibility. We assume an extended source over the XIS FOV whose surface brightness is comparable to that of the CXB. We also assume an exposure time of 100 ks, typical for this type of extended source. Such observation typically spans two days, corresponding to an NTE exposure of 5 ks in our database. We will concentrate on the energy band of 5-12 keV of the XIS-FIs. We find the count rate of the NXB, I_{NXB} , to be 5.0×10^{-2} cts s⁻¹ and the reproducibility, ΔI_{NXB} , to be 1.8×10^{-3} cts s⁻¹ (3.5 % of the I_{NXB}) based on table 5(c). Kushino et al. (2002) measured a CXB power-law photon index of 1.412 and flux of $6.38 \times 10^{-8} \text{ erg cm}^{-2} \text{ s}^{-1} \text{ sr}^{-1}$. They also estimated the spatial fluctuation of the CXB flux to be 6.5% (1 σ) by analyzing the ASCA GIS data. Employing these values, we can evaluate the expected count rate for the XIS-FIs, I_{CXB} , to be 9.7×10^{-3} cts s⁻¹. We assume that the spatial fluctuation follows to the Poisson statistics of the number of sources in the FOV. Then, we can calculate the spatial fluctuation of the CXB for the XIS FOV to be $6.5 \times \sqrt{0.4/0.088} = 14\%$, since the FOVs of the ASCA GIS and the XIS are 0.4 deg² and 0.088 deg², respectively. Employing the exposure of 100ks, we can estimate the CXB fluctuation in the XIS, ΔI_{CXB} , to be 1.4×10^{-3} cts s⁻¹. We should note that ΔI_{CXB} is comparable to ΔI_{NXB} in our case.

When we obtain the count rate of the raw data, I_{raw} , we will subtract the NXB and CXB from it in order to evaluate the source count rate, I_{src} . Since we assume I_{src} to be comparable to I_{CXB} , I_{raw} is $(5.0 + 0.97 + 0.97) \times 10^{-2} = 6.9 \times 10^{-2}$ cts s⁻¹ and its statistical error, ΔI_{raw} , is 8.3×10^{-4} cts s⁻¹. We will obtain I_{src} by subtracting $(I_{CXB} + I_{NXB})$ from I_{raw} . We can calculate the error of I_{src} , ΔI_{src} , to be $\sqrt{\Delta I_{NXB}^2 + \Delta I_{CXB}^2 + \Delta I_{raw}^2} = 2.4 \times 10^{-3}$ cts s⁻¹. ΔI_{NXB} and ΔI_{CXB} contribute almost equally to ΔI_{src} , while the contribution of the statistical error ΔI_{raw} is smaller than these two. Similarly, we evaluate the NXB reproducibility of the XIS-FIs in the 1-7 keV energy band by using the same method as employed in the 5-12 keV band. The calculations show that $\Delta I_{NXB} = 1.7 \times 10^{-3}$, $\Delta I_{CXB} = 8.1 \times 10^{-3}$, and $\Delta I_{src} = 1.3 \times 10^{-3}$ (cts s⁻¹). We should note that I_{NXB} does not change so much while I_{CXB} is 6 times bigger in the 1-7 keV band than that in the 5-12 keV band. Therefore, ΔI_{src} is mainly determined by ΔI_{CXB} rather than by ΔI_{NXB} .

5.2. Case study: filtering the data to reduce the error of source count rate

We have considered the case of a 100 ks exposure in the subsection above. Depending on the exposure time and the count rate of the source, the contribution of the statistical error, ΔI_{raw} , to ΔI_{src} is minor. ΔI_{src} can be reduced in some conditions by filtering the data as shown below.

We consider a specific example in which the data are filtered with the condition of PIN-

UD < 225 cts s⁻¹. We call this as the "PIN-UD filter". Using the PIN-UD filter, the exposure time reduces to 85 % of that without the filter. The NXB count rate and reproducibility in the 5-12 keV band of the XIS-FIs are 4.6×10^{-2} cts s⁻¹ (I'_{NXB}) and 3.2 % (normalized by I'_{NXB}), respectively. These values are based on the NXB2 data, and this reproducibility is obtained for each 5 ks exposure.

We will derive the condition that the PIN-UD filter provides a smaller ΔI_{src} than that without the PIN-UD filter for a given on-source observation. We hereafter refer to the error of source count rate and the NXB reproducibility with the PIN-UD filter as $\Delta I'_{src}$ and $\Delta I'_{NXB}$, respectively. On the other hand, those without the PIN-UD filter are newly defined as ΔI_{src} and ΔI_{NXB} , respectively. $\Delta I'_{src}$ is expressed as below,

$$\Delta I'_{src}^{2} = \Delta I'_{NXB}^{2} + \Delta I_{CXB}^{2} + \Delta I'_{raw}^{2}, \tag{8}$$

$$= (0.032I'_{NXB})^2 + \Delta I_{CXB}^2 + \frac{I_{CXB} + I'_{NXB} + I_{src}}{0.85T} , \qquad (9)$$

where $\Delta I'_{raw}$ is the statistical error of the count rate of the raw data with the PIN-UD filter. T is the exposure time of the on-source observation. On the other hand, ΔI_{src} is expressed as below,

$$\Delta I_{src}^2 = (0.035 I_{NXB})^2 + \Delta I_{CXB}^2 + \frac{I_{CXB} + I_{NXB} + I_{src}}{T} \ . \tag{10}$$

 I_{src} , I_{CXB} , and ΔI_{CXB} are not altered by the PIN-UD filter. To obtain a value for $\Delta I'_{src}$ which is smaller than that for ΔI_{src} , the condition is expressed as below,

$$(0.032I'_{NXB})^2 + \frac{I_{CXB} + I'_{NXB} + I_{src}}{0.85T} < (0.035I_{NXB})^2 + \frac{I_{CXB} + I_{NXB} + I_{src}}{T} , \qquad (11)$$

$$I_{src} < 5.1 \times 10^{-3} \left(\frac{T}{1 \,\text{ks}}\right) - 0.033 \,\text{cts s}^{-1} \,.$$
 (12)

The term of ΔI_{CXB}^2 vanishes from both sides of the above inequality.

In the case that the exposure time of the on-source observation is $100 \,\mathrm{ks}$, the PIN-UD filter is effective for a diffuse source whose count rate is less than $0.48 \,\mathrm{cts} \,\mathrm{s}^{-1}$. This count rate corresponds to 49 times that of the CXB. On the other hand, if the exposure time is $20 \,\mathrm{ks}$, the PIN-UD filter is effective only for a source whose count rate is lower than 7.1 times of that of the CXB.

6. Summary

We have constructed the NXB database by collecting the XIS events of the NTE. The NXB database, accompanied with EHK files, and two software tools, $mk_corsorted_spec_v1.0.pl$ and $mk_corweighted_bgd_v1.1.pl$, are now accessible via the Suzaku web page at ISAS/JAXA and GSFC/NASA. Since the XIS NXB depends on the cut-off-rigidity in orbit or on the PIN-UD count rate, we need to equalize the distributions of these parameters for the on-source observations and for the NTE observation so that we can actually subtract the NXB. We

have examined two modeling parameters to model the NXB, the COR2 and the PIN-UD. We find large deviation of the NXB count rate from that expected from both models when Suzaku passes through high altitude and high latitude regions. Excluding those data, the NXB reproducibilities are significantly improved. Similarly, excluding the data taken in September 2005, the reproducibility for the XIS2 is improved. Our results show that the NXB model sorted by the PIN-UD has better reproducibility than that by the COR2. Using the NXB data in 5 ks exposure bins, the reproducibility obtained with the PIN-UD model is 4.55-5.63% for each XIS NXB in the 1-7 keV band and 2.79-4.36% for each XIS NXB in the 5-12 keV band. This NXB reproducibility in 5-12 keV, 1.8×10^{-3} cts s⁻¹, is comparable to the spatial fluctuation of the CXB for the XIS FOV, 1.4×10^{-3} cts s⁻¹. The NXB reproducibility and the spatial fluctuation of the CXB are evaluated to be 1.7×10^{-3} cts s⁻¹ and 8.1×10^{-3} cts s⁻¹, respectively, in the 1-7 keV band. Depending on the exposure time and the count rate of the source, the statistical error of the raw data is much smaller than the NXB reproducibility. In such a case, the error of the source count rate can be reduced by excluding the data with high NXB count rate (e.g. filtering with PIN-UD < 225 cts s⁻¹).

The authors wish to thank all the XIS team members for their support, help, and useful information. This work is partly supported by a Grant-in-Aid for Scientific Research by the Ministry of Education, Culture, Sports, Science and Technology (16002004 and 1910350). This study is also carried out as part of the 21st Century COE Program, 'Towards a new basic science: depth and synthesis'. N. T. is supported by JSPS Research Fellowship for Young Scientists.

Appendix 1. New and old map for the cut-off-rigidity

The cut-off-rigidity values have been calculated from the orbital position of Suzaku using a cut-off-rigidity map shown in Fig. 12(a). However, the map assumes charged particles originating from the zenith direction at an altitude of 500 km, and it uses an international geomagnetic reference field for 1975. This cut-off-rigidity definition (hereafter "COR") is out of date and inaccurate. We therefore define a new cut-off-rigidity map based on the recent cut-off-rigidity database.

The new cut-off-rigidity map is calculated by using corrected geomagnetic (CGM) coordinates. The CGM coordinates are useful to study geophysical phenomena affected by the Earth's magnetic field and are provided at the web service by NASA⁵ (Tsyganenko 1996). To calculate the CGM coordinates, several parameters are required. We set these parameters as follows; altitude is 570km, date is 2006/01/01~00:00:00, and default parameters are employed for the solar wind (Den = 3, Vel = 400, BY = 5, BZ = -6, and Dst = -30). Then, the new cut-off-rigidity value, R_C , is calculated as follows,

⁵ The service is available at \(\lambda\) http://modelweb.gsfc.nasa.gov/models/cgm/t96.html\(\rangle\)

$$R_C = 14.5 \frac{\cos^2 \theta}{r^2} \quad \text{GV}, \tag{A1}$$

where θ is the latitude in CGM coordinates. r is the distance from the center of earth's magnetism, and the value of r is normalized by the radius of the earth. We call this cut-off-rigidity as "COR2". Figure 12(b) shows the COR2 map. In the red box region shown in Fig. 12(b), since the CGM cannot be obtained due to the local magnetic structure, we use geomagnetic latitude obtained with dipole approximation in place of the CGM.

The cut-off-rigidity value for each event can be determined from the EHK file associated with each observation. The EHK files before revision 2.0 processing contain only the COR, while those after revision 2.0 contain both the COR and the COR2. These COR and COR2 values are calculated using the cut-off-rigidity maps of $rigidity_20000101.fits$ and $rigidity_20060421.fits$ in the generic area of the calibration database (CALDB).

Fig. 12. Maps of (a) the COR and (b) the COR2. The region A is -90° < latitude < 45° , and the region B encompasses the remaining latitude range.

We evaluate the reproducibility of the NXB model with the COR by the same way as that with the COR2 or the PIN-UD in main text. The bin ranges of the COR to sort the NXB data and on-source data are the same as the COR2 as shown in table 3. Table 8 shows the reproducibility of the NXB model with the COR in the energy bands of 1-7 keV and 5-12 keV. The reproducibility is calculated by dividing the NXB2 data into 5 ks or 50 ks exposure bins. We found that the COR has the worst reproducibility among the three kinds of the NXB models.

We searched for the location where the COR does not perfectly reproduce the XIS NXB. Figure 13(1) shows the average count rate of the XIS0 NXB in the 5-12 keV energy band as a function of the three modeling parameters, in the northern hemisphere and in the southern hemisphere, displayed separately. This count rate is obtained from the NXB2 data. For the three modeling parameters, there is not a large difference between the NXB count rate in the

northern hemisphere and that in the southern hemisphere. On the other hand, if we take the data from two different longitude regions, region A and region B in Fig. 12, we obtain Fig. 13(2). There is a significant difference between the NXB count rate in region A and that in region B for a given value of the COR. This is one reason the COR gives the worst reproducibility.

Table 8. Reproducibility of the NXB model with the COR in the energy bands of 1-7 keV and 5-12 keV.

Sensor	Reproducibility of COR (%)				
	$5 \mathrm{ks}$ exposure			$50\mathrm{ks}$ exposure	
	$1-7 \mathrm{keV^*} \qquad 5-12 \mathrm{keV^\dagger}$			$1\text{-}7\mathrm{keV^*}$	$5-12\mathrm{keV}^\dagger$
XIS0	5.73 ± 0.76	4.46 ± 0.64		2.28 ± 0.88	1.60 ± 0.72
XIS1	7.97 ± 0.73	6.60 ± 0.51		3.42 ± 0.94	3.12 ± 0.75
XIS2	7.63 ± 0.85	5.60 ± 0.68		1.70 ± 0.84	2.02 ± 0.77
XIS3	6.58 ± 0.85	3.20 ± 0.65		2.14 ± 0.92	1.15 ± 0.72

^{*} These values are normalized by the average count rates shown in table 6.

Fig. 13. NXB of the XISO for given values of (a) COR, (b) COR2, and (c) PIN-UD. (1) shows the NXB count rates for the northern and southern hemisphere separately. Open circles are for the north hemisphere and open squares for the south hemisphere. (2) shows the count rates for region A and region B (see Fig. 12). Open circles are for region A and open squares for region B.

Appendix 2. Errors of the statistical parameters

We discuss the errors of σ_c , $\sigma_{sta,c}$, $\sigma_{sys,c}$, and $\sigma_{sys,\Delta c}$ as defined in section 3.2. If the distribution of C_j follows a Gaussian distribution whose average and standard deviation are μ and σ respectively, then $(n-1)\sigma_c^2/\sigma^2 \equiv X$ follows a χ^2 distribution with (n-1) degrees of

 $^{^\}dagger$ These values are normalized by the average count rates shown in table 4.

freedom. The expected value and variance of X are (n-1) and 2(n-1), respectively. Although the distribution of the statistical error of X does not correctly follow a Gaussian distribution, the statistical error can be approximated with $\sqrt{2(n-1)}$. Thus, the statistical error of σ_c^2 is $\sigma^2 \sqrt{2/(n-1)}$. However, since σ is a standard deviation of the parent population and can not be obtained, we approximate that σ equals σ_c . As a result, the statistical error of σ_c^2 is $\sigma_c^2 \sqrt{2/(n-1)}$. The statistical error of σ_c ($\Delta \sigma_c$) is expressed by using the principle of error propagation as follows,

$$\Delta \sigma_c = \frac{\sigma_c}{\sqrt{2(n-1)}} \ . \tag{A2}$$

In the same way, the statistical error of $\sigma_{sta,c}$ ($\Delta \sigma_{sta,c}$) is obtained as follows,

$$\Delta \sigma_{sta,c} = \frac{\sigma_{sta,c}}{\sqrt{2(n-1)}} \ . \tag{A3}$$

The statistical errors of $\sigma_{sys,c}$ ($\Delta\sigma_{sys,c}$) is expressed by using the principle of error propagation as follows,

$$\Delta \sigma_{sys,c} = \frac{1}{\sigma_{sys,c}\sqrt{2(n-1)}} \sqrt{\sigma_c^4 + \sigma_{sta,c}^4} \ . \tag{A4}$$

In the same way as $\Delta \sigma_{sys,c}$, the statistical error of $\sigma_{sys,\Delta c}$ ($\Delta \sigma_{sys,\Delta c}$) is expressed as follows

$$\Delta \sigma_{sys,\Delta c} = \frac{1}{\sigma_{sys,\Delta c} \sqrt{2(n-1)}} \sqrt{\sigma_{\Delta c}^4 + \sigma_{sta,\Delta c}^4} \ . \tag{A5}$$

References

Burke, B. E., Mountain, R. W., Harrison, D. C., Bautz, M. W., Doty, J. P., Ricker, G. R., & Daniels, P. J. 1991, IEEE Trans. ED, 38, 1069

Carter, J. A. & Read, A. M. 2007, ApJ, 464, 1155

Fujimoto, R., et al. 2007, PASJ, 59, S133

Fujita, Y., Tawa, N., Hayashida, K., Takizawa, M., Matsumoto, H., Okabe, N., & Reiprich, T. H., 2007, PASJ, in press (astro-ph/07052017)

Hasinger, G., et al. 2001, A&A, 365, 45

Ishisaki, Y., et al. 2007, PASJ, 59, S113

Kokubun, M., et al. 2007, PASJ, 59, S53

Koyama, K., et al. 2007, PASJ, 59, S23

Kushino, A., Ishisaki, Y., Morita, U., Yamashita Y. N., Ishida, M., Ohashi, T., & Ueda, Y. 2002, PASJ, 54, 327

Lumb, D. H., et al. 2000, Proc. SPIE, 4140, 22

Mitsuda, K., et al. 2007, PASJ, 59, S1

Mizuno, T., Kamae, T., Godfrev, G., Handa, T., Thompson, D. J., Lauben, D., Fukazawa, Y., & Ozaki, M. 2004, ApJ, 614, 1113

Snowden, S. L., et al. 1997, ApJ, 485, 125

Takahashi, T., et al. 2007, PASJ, 59, S33

Tsyganenko, N. A. 1996, Proc. Third Int. Conf. on Substorms (ICS-3), Versailles, France, 12-17 May 1996, ESA SP-389

Weisskopf, M. C., Brinkman, B., Canizares, C., Garmire, G., Murray, S., & Van Speybroeck, L. P. 2002, PASP, 114, 1

Yamaguchi, H., et al. 2006, Proc. SPIE, 6266, 626642